Mechanical properties and strengthening mechanisms of Al-15%B_4C composites with Sc and Zr at elevated temperatures

Jian Qin, Zhan Zhang, X.-Grant Chen *

Department of Applied Science, University of Quebec at Chicoutimi,

Saguenay (QC), Canada G7H 2B1

Abstract

The mechanical properties at ambient and elevated temperatures of two Al-15 vol.% B_4C composites, S40 with 0.4 wt.% Sc and SZ40 with 0.4 wt.% Sc and 0.24 wt.% Zr, are investigated during long-term thermal annealing. The presence of large B_4C particles in the microscale has a moderate but stable strengthening effect on Al-B_4C composites at ambient and elevated temperatures, while the precipitation of nanoscale Al_3Sc and Al_3(Sc, Zr) in the composite matrix provides a predominate contribution to the composite strength, which is varied by tested temperatures. The Al_3Sc precipitates in S40 remain coarsening-resistant at 523 K (250 °C), whereas the Al_3(Sc, Zr) precipitates in SZ40 are thermally stable at 573 K (300 °C) over 2000 h of annealing. At higher annealing temperatures (573 K (300 °C) for S40 and 623 K (350 °C) for SZ40), both Al_3Sc and Al_3(Sc, Zr) precipitates become coarsening with prolonged annealing time. The yield strength of S40 and SZ40 at ambient temperature decreases with increasing precipitate size, which can be explained by the classical precipitate shearing and Orowan bypass mechanisms. At elevated temperatures (523−623 K (250-350 °C)), considerably lower yield stresses are observed compared to those at ambient temperature, which invokes a dislocation climb mechanism. The predicted yield strengths at elevated temperatures by the combination of dislocation climb and Orowan models are in good agreement with the experimental data.

Keywords: Mechanical properties; Al-B_4C composites; Sc and Zr; Strengthening mechanism; High temperature stability.

* Corresponding author, Tel.: 1 418 545 5011 ext. 2603, E-mail: xgrant_chen@uqac.ca (X.-G. Chen).

1. Introduction

Al-B_4C metal matrix composites (MMCs) have been widely used as neutron absorber materials in the transport and storage of spent nuclear fuels in the nuclear industry because of the special capacity of B_4C for excellent neutron absorption [1, 2]. In service, the composites can be exposed at elevated temperatures (523−623 K (250−350 °C)) for extended periods of time, owing to the heat generation and accumulation by absorbing thermal neutrons from the spent fuels [1, 3]. To improve the overall performance of the neutron absorber materials, it is desirable to maximize the operating temperature and thermal stability of materials at such high temperature. As the matrix of MMCs, most commercial precipitation-strengthened 2xxx, 6xxx and 7xxx aluminum alloys are limited to be used below 473 K (200 °C). The mechanical properties of these matrices can be seriously deteriorated at higher temperature because of rapid coarsening of their precipitates (overaging effect) [4]. For precipitation-strengthened aluminum alloys, Al-Sc alloy is a rare exception, which can be used up to 573 K (300 °C) because it can form nanoscale coherent Al_3Sc precipitates with a low coarsening rate [5]. Above this temperature, Al_3Sc precipitates may coarsen and lose coherency, which results in the degradation of mechanical properties of materials [6, 7]. It was reported that Zr could partially substitute Sc to form $Al_3(Sc_{1-x}Zr_x)$ precipitates with better coarsening resistance [8, 9], which improves the thermal stability of precipitates up to 623 K (350 °C) [9] and increases the strength and recrystallization resistance [10-12]. Compared to Sc, Zr has lower diffusivity, and its substitution forms a shell at the α-Al/$Al_3(Sc_{1-x}Zr_x)$ interfaces, which inhibits Sc diffusion [13-15]. Moreover, Zr can decrease the lattice parameter of the Al_3Sc precipitates, which decreases the lattice parameter misfit [16]. Thus, Zr decreases the coarsening rate of precipitates and benefits the thermal stability of materials [17].

In our previous works [18, 19], the mechanical properties of Al-B_4C (15 - 30 vol.% B_4C) MMCs without alloying at elevated temperatures have been investigated. The reinforcement of B_4C particles and their interfaces with Al matrix were very stable at high temperature. The presence of B_4C particles can provide an additional strengthening to Al matrix at both ambient and elevated temperatures. The strengthening mechanisms of reinforcements in MMCs can be divided into two categories, direct and indirect strengthening. The former refers to the load transfer from the weak matrix, across the matrix/reinforcement interface, to the higher stiffness reinforcement. And the latter involves dislocations accumulation around the reinforce particles due to the thermal expansion mismatch [20]. However, due to large particle size of B_4C particles (in the micrometer scale), their contribution to the overall composite strength was limited. To further improve the strength at elevate temperatures, the microstructure and mechanical properties of Al-B_4C MMCs with Sc and Zr additions have been studied [7, 18, 19, 21]. To facilitate the manufacture of Al-B_4C composites, the addition of a certain amount of Ti was necessary to prevent the degradation of B_4C with liquid Al using a liquid-mixing process [22]. Ti could also significantly reduce the consumption of Sc and Zr in the interface reactions and enable most of the Sc and Zr amounts to be retained in the matrix for precipitation strengthening [23]. The results of our previous study [7] demonstrated that the yield strength at ambient temperature of Al-B_4C MMCs with Sc and Zr was thermally stable at 523-573 K (250-300 °C) up to 2000 h. However, there is currently limited information available in the literature about the mechanical properties and their thermal stability at elevated temperatures ($T > 0.5$ Tm (the absolute melting temperature of the alloy)) of Al alloys and composites with Sc and Zr.

The present study examines the mechanical properties and their thermal stability of Al-B_4C MMCs with Sc and Zr addition at elevated temperatures ($T > 0.5$ Tm, particularly in the range of 523−623 K (250−350 °C), which are correlated with the microstructural evolution during

long-term thermal annealing. The study also aims to identify the governing strengthening mechanisms at elevated temperature and verify with experimental results, which will be used for future development of high-temperature, thermally stable Al-base MMCs.

2. Experimental procedure

Two experimental Al 1100-15 vol.% B_4C composites, namely S40 with 0.4 wt.% Sc and SZ40 with 0.4 wt.% Sc plus 0.24 wt.% Zr, were prepared for this investigation. In addition, an unalloyed Al 1100-15 vol.% B_4C composite without Sc and Zr as a base material was prepared to compare the effect of the precipitates on mechanical properties. Their nominal chemical compositions are listed in Table 1.

In the composite melt preparation, commercial pure aluminum (99.7%) was first melted in an electric resistance furnace. The preheated master alloys, Al-2 wt.% Sc, Al-15 wt.% Zr, Al-10 wt.% Ti were then added into the aluminum liquid and held at 1073 K (800 °C) for 40 minutes to encourage the dissolution of master alloys. Prefabricated Al 1100-25 vol.% B_4C with 2.0 wt.% Ti cast ingots, supplied by Rio Tinto Alcan, were subsequently introduced into the alloyed melt. Ti is deliberately added to limit the Al/B_4C interface reaction during Al-B_4C composite preparation [22]. The average size of the B_4C particles (F360) was 23 μm. The composite melt was held at 1013 K (740 °C) for 30 minutes with mechanical stirring to ensure a uniform distribution of B_4C particles in the melt, and then cast into a preheated permanent steel mold with a dimension of 30×40×80 mm.

To obtain the precipitation strengthening, the cast ingots of S40 were homogenized at 913 K (640 ºC) for 24 h whereas SZ40 were treated at 913 K (640 ºC) for 96 h, and then quenched in water at room temperature. The homogenized samples of S40 and SZ40 were aged at 573 K (300 ºC) for 24 h, at which the hardness or yield strength of the composites reached the maximum

values [21]. The applied heat treatment processes were based on our previous works [7, 21] and the peak aging paraments are listed in Table 2. The unalloyed Al 1100-15 vol.% B_4C samples (the base composite) were tested in the as-cast condition due to its non-heat-treatable nature. Moreover, to evaluate the long-term thermal stability, S40 and SZ40 samples on the peak aging condition were annealed at elevated temperatures (523 to 623 K (250 to 350 °C)) up to 2000 hours (Table 2).

Compression tests were performed on a Gleebe 3800 thermo-mechanical testing unit with a strain rate 10^{-3} s^{-1} to determine the 0.2% offset yield strength (YS) at ambient and elevated temperatures based on ASTM E9-89a standard. The samples were deformed to a total true strain of 0.2. The dimensions of the cylindrical specimens for compression tests are 15 mm in length and 10 mm in diameter. An average value of yield strength was obtained from five compression tests. Vickers microhardness was also used to assess the mechanical properties at ambient temperature (298K (25°C)) with a load of 25 g and indentation time of 15 s on polished surface. A minimum of 20 measurements were performed on the composite matrix of each sample, from which the mean value and standard deviation were calculated.

The microstructures of the experimental composites were examined by an optical microscope, a scanning electronic microscope (SEM, JSM-6480LV), and a transmission electron microscope (TEM, JEM-2100). For TEM sample preparation, a 500-μm-thick specimen was first sliced from the composite samples, from which 3-mm-diameter discs were punched. TEM disc foils were prepared by metallographic grinding and polishing as well as dimpling, followed by milling using a Gatan PIPS (Model 691). Centered dark-field images of the precipitates were recorded using the {100} superlattice reflections near the <011> direction on two-beam diffraction conditions. Convergent-beam electron diffraction (CBED) patterns were used to measure the thickness of the TEM specimens. The precipitate volume fractions and the

equivalent diameters were determined using image analysis on TEM images. To consider the precipitate truncation effect in TEM images, the method in [24] was used for the calculation of volume fraction. To reveal the grain boundaries of the matrix under optical microscoper, some of samples were polished and etched with a 0.5%HF solution. Grain size was evaluated following ASTM E112 standard.

3. Results

3.1 Microstructure characterization

Fig. 1 shows the typical microstructure of Al 1100-15 vol.% B_4C composites in an example of S40. The B_4C particles were uniformly distributed in the Al matrix (Fig. 1a), and particle clusters were rarely found. The Al matrix of the composites has all coarse grains, and the average grain sizes are approximately 100 μm in SZ40 and 130 μm in S40 at the peak aging condition. At high magnification (Fig. 1b), some small reaction-induced particles, which were generated during the melt preparation such as TiB_2, Al_3BC, ScB_2 and Al_3ScC (identified in [23]), are observed around the B_4C particles. During the long-term thermal annealing at the temperature range of 523−623 K (250−350 °C), the B_4C ceramic particles and Al grains were notably stable. The variation of grain sizes for both S40 and SZ40 before and after 2000 h annealing was less than 0.8%.

The precipitation evolution of the S40 and SZ40 composites under the peak aging condition and long-term annealing was examined using TEM. Fig. 2 shows representative TEM micrographs at different thermal-treatment conditions. At the peak aging condition (Figs. 2a and 2d), fine and coherent Al_3Sc and Al_3(Sc, Zr) precipitates of S40 and SZ40 composites were formed in the Al matrix with a high number density. Most Al_3Sc and Al_3(Sc, Zr) precipitates exhibit a spherical morphology and homogeneously distribute in the Al matrix. The volume

fraction of the Al_3Sc precipitates in S40 is approximately 0.24% with an average radius of 1.7 ± 0.7 nm, whereas the volume fraction of Al_3(Sc Zr) in SZ40 is approximately 0.33% with an average radius of 1.1 ± 0.32 nm.

During the long-term annealing at high temperatures, precipitate coarsening can be observed. For the S40 composite, annealing at 523 K (250 °C) for 2000 h yielded an average precipitate radius of only 2.1 ± 0.59 nm (Fig. 2b), whereas annealing at 573 K (300 °C) for 2000 h yielded a precipitate radius of 6.1 ± 2.34 nm (Fig. 2c), which indicates that the precipitate coarsening in S40 only becomes obvious at 573 K (300 °C). Meanwhile, the average precipitate radius of the SZ40 composite is approximately 1.4 ± 0.32 nm after 2000 h at 573 K (300 °C) (Fig. 2e), and it grows to 4.5 ± 1.48 nm after annealing at 623 K (350 °C) for 2000 h (Fig. 2f). Fig. 3 shows the precipitate coarsening curves as a function of annealing time for both S40 and SZ40 composites. Compared to the Al_3Sc precipitates in S40, the Al_3(Sc, Zr) precipitates in SZ40 exhibit a low coarsening rate even at higher temperatures. It is to notice that the standard deviation of Al_3Sc radius is larger than that of Al_3(Sc, Zr) in Fig. 3, mainly due to high coarsening rate of Al_3Sc. The precipitate coarsening behaviors in both S40 and SZ40 composites can be described using Lifshitz-Slyozov-Wagner **(**LSW) equation [25-27]:

$$\bar{r}_t^{\,3} - \bar{r}_o^{\,3} = at \quad (1)$$

where $\bar{r}_o$ is the mean initial precipitate radius, $\bar{r}_t$ is the precipitate radius at time *t*, and *a* is the coarsening rate constant, which is related to the temperature and material composition [16, 28, 29].

The coarsening rate constants *a*, which are experimentally determined in Fig. 3, are 1.30×10^{-33} m^3s^{-1} at 523 K (250 °C) and 3.16×10^{-32} m^3s^{-1} at 573 K (300 °C) for the S40 composite. For the SZ40 composite, the constant values are 1.27×10^{-33} m^3s^{-1} at 573 K (300 °C) and 1.19×10^{-32} m^3s^{-1} at 623 K (350 °C). The results imply that during prolonged exposure at elevated

service temperatures, the $Al_3(Sc,Zr)$ precipitates in SZ40 are more thermally stable and coarsening-resistant than the $Al_3(Sc)$ precipitates in S40, which is confirmed by similar observations in other Sc- and Zr-containing aluminum materials [8, 21].

3.2 Mechanical properties as a function of temperature

The yield strengths of four different materials were evaluated at various temperatures, as showed in Fig. 4a. The true stress-train curves of three Al-15%B_4C MMCs obtained from compression tests are displayed in Figs. 4b-d, from which the 0.2% offset yield strengths are determined. All measured yield strengths are listed in Table 3. In general, the yield strength of aluminum, including the AA1100 alloy and the matrix of the base composite, decreases with the increase in test temperature mainly due to the decrease in aluminum shear modulus with increasing temperature [30]. The measured yield strength of the base Al-15%B_4C composite at ambient temperature is 46 MPa, which is approximately 12 MPa above that of the AA1100 alloy (commercially pure Al). With increased tested temperature, the increment of the yield strength of the base composite slightly decreases and remains about 10 MPa at 573 K (300 °C).

Meanwhile, the composites alloyed with Sc (S40) and Sc and Zr (SZ40) have much higher strengths than the base composite, particularly at ambient temperature. The yield strengths of S40 and SZ40 are 141 MPa and 165 MPa, respectively, at ambient temperature. Precipitated during the aging treatment, the high number density of nanoscale precipitates Al_3Sc and $Al_3(Sc, Zr)$ effectively strengthens the composites at ambient temperature. At elevated temperatures (523−623 K (250−350°C)), the yield strength dramatically decreases with increasing temperature. For example, at 573 K (300 °C), the yield strengths of S40 and SZ40 are reduced to 46 and 54 MPa, respectively. SZ40 generally has higher yield strength than S40 mainly because of a higher volume fraction of precipitates.

It should be mentioned that even at high temperatures (523−623 K (250−350°C)), the yield strengths of S40 and SZ40 are still much higher than that of the base Al-15%B_4C composite. It indicates that Al_3Sc and Al_3(Sc, Zr) precipitates in Al matrix provide the predominate contribution to the overall composite strength. The presence of large B_4C particles in the tens micrometers can only moderately contribute to the composite strength, which is mainly attributed to the load transfer from the soft matrix onto the hard reinforcement and dislocation accumulation around reinforce particles due to thermal expansion mismatch between the matrix and the reinforcement particles [31].

The overall strength σ_t of a material, which includes various characteristic strength increment $\Delta\sigma_i$, can be described by the empirical Eq. (2) with an exponent $1 \leq k \leq 2$ [32].

$$\sigma_t^k = \sum_i \Delta\sigma_i^k \tag{2}$$

For Al-B_4C composites with Al_3Sc and Al_3(Sc, Zr) precipitates, the precipitate strength increments can be calculated using Eq. (3):

$$\Delta\sigma_p = \left(\sigma_t^k - \sigma_{Al+15\%B_4C}^k\right)^{1/k} \tag{3}$$

where σ_{Al+B_4C} is the strength contributed by the unalloyed Al-15%B_4C composite, and $\Delta\sigma_p$ is the strength increment attributed to the precipitates. It has been reported that *k* is equal to 1 for an Al-2 wt.% Mg alloy that was strengthened by nanoscale Al_3Sc precipitates [33]. In the present study, we adapted *k*=1 to calculate all yield strength increments contributed by precipitates.

3.3 Thermal stability during long-term thermal holding

The mechanical properties at ambient temperature after long-term thermal holding at various temperatures were evaluated using Vicker's hardness measurement (Fig. 5). The results in Fig. 5

show that the microhardness of two Sc- and Zr-containing composites remains notably stable up to 2000 h at lower exposure temperatures (523 K (250 °C) for S40 and 573 K (300 °C) for SZ40), whereas the microhardness of both materials remarkably decreases with prolonged holding time at higher exposure temperatures (573 K (300 °C) for S40 and 623 K (350 °C) for SZ40). For example, the microhardness of the S40 composite at 573 K (300 °C) decreases after 500 h of holding, and its value decreases from 65 HV at the beginning of holding to 54 HV after 2000 h of holding.

At lower exposure temperatures, the precipitates in both composites (Al_3Sc in S40 and Al_3(Sc, Zr) in SZ40) exhibit notably limited coarsening (Fig. 3); thus, both composites exhibit excellent softening resistance (up to 523 K (250 °C) for S40 and 573 K (300 °C) for SZ40). At higher exposure temperatures, the Al_3Sc and Al_3(Sc, Zr) precipitates slowly coarsen with time, which weakens the material strength and causes the progressive softening during the prolonged thermal holding. A similar tendency of the mechanical properties of Al-B_4C composites with Al_3Sc and Al_3(Sc, Zr) precipitates at ambient temperature was also observed in the previous study [7]. It is also evident that the addition of Zr into the Sc-containing composite improves the softening resistance and delays the material softening towards higher temperature.

To evaluate the mechanical properties at elevated temperatures, compression tests were performed at the same temperatures as the sample-annealing temperatures. Fig. 6a shows the yield strength of S40 as a function of the holding time at two tested temperatures. At both temperatures (523 and 573 K (250 and 300 °C)), the yield strength first increases in the initial 500 h and tends to stabilize up to 2000 h. The yield strength of SZ40 remains unchanged from the beginning of holding till 2000 h at 573 (300) and 623 K (350 °C) (Fig. 6b). At lower exposure temperatures during annealing, both precipitates in S40 and SZ40 were practically stable against coarsening (Fig. 3). Thus, the yield strength at elevated temperatures remains

stable during the entire annealing period (2000 h). However, at higher exposure temperatures (573 K (300 °C) for S40 and 623 K (350 °C) for SZ40), the Al_3Sc and $Al_3(Sc, Zr)$ precipitates in both composites coarsened with prolonged holding time. It is surprising to observe constant and stable yield strengths at such high temperatures. On the other hand, for long-term service as neutron absorber materials, the Al-B_4C composite with Sc (S40) can generally sustain stresses on the order of 50 MPa at $0.61T_m$ (573 K (300 °C)), while the SZ40 composite can be further operated under stresses on the order of 40 MPa at $0.67T_m$ (623 K (350 °C)).

Based on the results of mechanical properties at various temperatures and their evolution during long-term thermal holding, a few interesting phenomena are observed: (1) the yield strength increment of two composite materials dramatically decreases with increasing test temperature; (2) during the long-term holding at high temperatures (573 K (300 °C) for S40 and 623 K (350 °C) for SZ40), the mechanical properties at ambient temperature of the two composites gradually decrease with prolonged holding time because the Sc- and Zr-containing precipitates coarsen; (3) the mechanical properties at elevated temperatures remain thermally stable during 2000 h annealing and independent from the coarsening of Sc- and Zr-containing precipitates, unlike those tested at ambient temperature. This information suggests that the strengthening mechanisms of the precipitates can be different at ambient and elevated temperatures. To understand the mechanical properties at various temperatures and their thermal stability at high temperature, the possible strengthening mechanisms are outlined and discussed below.

4. Discussion

4.1 Strengthening mechanisms

For precipitation-strengthened materials that are operated at elevated temperature, both the ambient-temperature strength and high-temperature strength are essential for the overall performance of materials. The ambient-temperature strength can be generally explained and predicted by classical precipitate shearing and Orowan bypassing mechanisms [10, 17, 21, 30, 32, 34]. It is known that for a precipitate, which has a size smaller than the critical radius and has coherent structure with matrix, the strength is controlled by precipitate shearing, whereas for large precipitate sizes the Orowan dislocation bypass mechanism controls the strength. At elevated temperature, there is sufficient thermal energy to allow dislocation circumventing the precipitates by climbing. The dislocation climb mechanism may become active when deformed at elevated temperature with low strain rates because the vacancy diffusion becomes significant at temperature above $0.5T_m$ [35, 36]. Miura et al. [37] used the dislocation climb to explain the tensile deformation behavior of an Al-Sc alloy at temperatures between 298 K (25 °C) and 523 K (250 °C). To explain the creep properties of Al-Sc alloys at elevated temperature, Marquis et al [30, 35] introduced a dislocation climb mechanism and developed a model to predict the creep threshold stresses.

4.1.1 Dislocation climb mechanism

In precipitate-strengthened Al alloys, the interaction between the dislocation and the matrix mainly includes: (1) modulus mismatch; (2) lattice mismatch (coherency strengthening); and (3) order strengthening [10, 32, 34, 35]. For coherent precipitates, the repulse stress for dislocation climbing is caused by the elastic interaction between the dislocations and the precipitates [35]. The components of the elastic reaction are due to lattice mismatch and modulus mismatch [34, 35]. Therefore, the strength increment caused by dislocation climb strengthening, $\Delta\sigma_C$, is the sum

of $\Delta\sigma_{LMC}$ and $\Delta\sigma_{MMC}$, which are the strength increments of lattice mismatch and modulus mismatch, respectively.

To calculate $\Delta\sigma_{MMC}$, the force F that acts on the dislocation must be determined. Based on a model proposed by Marquis and Dunand for dislocation climbing over a coherent precipitate at elevated temperature [34, 35], a schematic of a dislocation at an initial location to climb over a precipitate is shown in Fig. 7. In fact, most of the Al_3Sc and $Al_3(Sc, Zr)$ precipitates exhibit a spherical morphology (Fig. 2). However, due to its complexity, there is no direct analytical solution for spherical morphology available in literature. A cylindrical form was selected [35, 38], because there is an analytical solution for a unit length of a straight dislocation to describe the interaction energy between a dislocation and an infinitely long cylinder, developed by Dundurs [39]. A cylinder-like particle with 2r in diameter and 2r in length (r is the cylinder radius) is taken as an approximation of a spherical particle (Fig. 7). The edge dislocation is at a distance, r+nb, away from the precipitate center; where b is the magnitude of the matrix burgers vector and n is a variable number which should be larger than 0.5 [35]. The dislocation position is determined by $y=cos\theta(r+nb)$ and $z_0+h=sin\theta(r+nb)$; where h is the distance between the dislocation glide plane and precipitate center, z_0 is the height of the dislocation segment climbed above its glide plane as shown in Fig. 7b and θ is the angle between the coordinate origin plane and the plane composed of the climbed dislocation segment. Based on the interaction energy for a unit length of an edge dislocation, the force between particles and dislocations can be calculated using Eq. 4 [39]:

$$F = -r\left(\frac{\partial E}{\partial y}\right) = \frac{G_m b^2}{\pi(k_m+1)(1-\beta^2)}\left\{2(\alpha+\beta^2)\frac{r^3 cos\theta}{(r+nb)((r+nb)^2-r^2)\,ln\,10}\right.$$
$$-[\alpha+\beta^2-2(1+\alpha)\beta]\frac{2r^3 cos\theta(cos^2\theta-sin^2\theta)}{(r+nb)^3} \quad (4)$$
$$\left.-(1+\alpha)\left[1-\beta-\frac{(1-\alpha)(1+\beta)}{1+\alpha-2\beta}\right]\frac{2r^3 cos\theta sin^2\theta}{(r+nb)^3}\right\}$$

E is the interaction energy for a unit length of an edge dislocation with precipitates [39]. According to Eq. (4), the force opposing dislocation glide is the greatest at $\theta=0$, i.e. $z_0+h=0$. Here, the initial position of a dislocation to climb a precipitate with a maximum repulsion force is at $\theta=0$ with a distance y=r+nb as shown in Fig. 7, and this dislocation initial position is applied for the prediction of mechanical properties in the study.

The dislocation is away from a precipitate with a distance y, and the expressions of α and β are as follows:

$$\alpha = \frac{\Gamma(k_m + 1) - (k_p + 1)}{\Gamma(k_m + 1) + k_p + 1} \tag{5}$$

$$\beta = \frac{\Gamma(k_m - 1) - (k_p - 1)}{\Gamma(k_m + 1) + k_p + 1} \tag{6}$$

G_m and G_p are the shear moduli of the matrix alloy and precipitates, respectively. The modulus mismatch parameter is defined as $\Gamma=G_m/G_p$; the Poisson parameters are: k_m=3-4ν_m and k_p=3-4ν_p, where ν is Poisson's ratio, and the subscripts m and p refer to the matrix and the particle, respectively [35, 39].

The critical resolved shear stress (CRSS) is described as [27]:

$$\tau = \frac{F^{\frac{3}{2}}}{\left(\frac{G_m b^2 2\pi}{3f}\right)^{\frac{1}{2}} br} \tag{7}$$

where f is the volume fraction of precipitates,

Then, the contribution of the modulus mismatch is [27]:

$$\Delta\sigma_{MMC} = M\tau = \frac{MF^{\frac{3}{2}}}{\left(\frac{G_m b^2 2\pi}{3f}\right)^{\frac{1}{2}} br} \tag{8}$$

Here, M is the mean matrix orientation factor, for aluminum, M=3.06 [40].

The contribution of the lattice mismatch is [27, 41]:

$$\Delta\sigma_{LMC} = \chi M(\varepsilon G_m)^{3/2}\sqrt{\left(2fb\langle r\rangle / G_m b^2\right)} \tag{9}$$

where χ=2.6 is a constant [27], and ε is the constrained strain. Here ε is [30]:

$$\varepsilon \approx \frac{2}{3}|\delta| \tag{10}$$

and,

$$\delta = \frac{a_p - a}{a} \tag{11}$$

where δ is related to the difference between the lattice parameters a_p and a of precipitate and matrix, respectively. The lattice parameter at 298 K (25 °C) is 0.4049 nm for Al and 0.4103 nm for Al_3Sc [16].

4.1.2 Orowan bypass mechanism

Orowan proposed the following strengthening mechanism: a dislocation loop appears around each particle when a dislocation bypasses precipitates [42]. This mechanism usually is operative for precipitates with larger sizes [21, 30]. The contribution in yield strength $\Delta\sigma_O$ due to this mechanism is determined by Eq. (12) [40]:

$$\Delta\sigma_O = \frac{0.4MG_m b \ln\left(\frac{2r}{b}\right)}{\pi\sqrt{1-\nu_m}\lambda} \tag{12}$$

where λ is the inter-precipitate distance, which is [32]:

$$\lambda = \left[\left(\frac{3\pi}{4f}\right)^{1/2} - 1.64\right] r \tag{13}$$

4.1.3 Shearing mechanism

For coherent precipitates with small sizes, the strength is controlled by the shearing mechanism, where a dislocation cuts and bypasses the precipitate. The precipitate strengthening has three main contributions: (i) modulus mismatch; (ii) lattice mismatch, and (iii) order strengthening. The strength increment $\Delta\sigma_s$, which is attributed to the shearing mechanism, is taken as the maximum value of modulus and lattice mismatches or the order strengthening [10]. Thus, they are described as follows [27]:

$$\Delta\sigma_{os} = 0.81M\frac{\gamma_{apb}}{2b}\left(\frac{3\pi f}{8}\right)^{1/2} \tag{14}$$

where $\Delta\sigma_{os}$ is the strength increment from order strengthening. γ_{apb} is the antiphase boundary (APB) energy per unit area on the slip plane, and $\gamma_{apb}\approx 0.5J/m^2$ [43-45].

$$\Delta\sigma_{MMS} + \Delta\sigma_{LMS} = 0.0055M\Delta G^{3/2}\left(\frac{2f}{Gb^2}\right)^{1/2} b\left(\frac{r}{b}\right)^{\frac{3m}{2}-1} + \chi M(\varepsilon G_m)^{3/2}\sqrt{\left(2fb\langle r\rangle / G_m b^2\right)} \tag{15}$$

Here, $\Delta\sigma_{MMS}$, and $\Delta\sigma_{LMS}$ are the contributions of the modulus mismatch and lattice mismatch to the strength increment in the shearing mechanism, respectively; m is a constant value of 0.85 [27].

4.2 Strengthening at ambient temperature

Fig. 8 shows the theoretical yield stresses at ambient temperature as a function of the precipitate size for both S40 and SZ40 composites based on the precipitate shearing and Orowan bypass mechanisms. The parameters in the calculation are listed in Table 4. In the theoretical stress curves, the yield strength sharply increases with the increase in precipitate size, when the shearing mechanism controls the process for the precipitate that is smaller than the critical value

(~2 nm), but the strength decreases with increasing precipitate size when the Orowan mechanism is dominant for the precipitate with radius larger than 2 nm.

The measured increments in yield strength at ambient temperature are included in Fig. 8. The data points were obtained from the compression tests and microhardness measurements using the relationship $\Delta\sigma_p \approx HV/3$ [49]. For the S40 and SZ40 samples at the peak aging condition, the experimental stress values were fitted in the shearing mechanism zone because the precipitate size is notably small. For the samples that were annealed at elevated temperatures (523−623 K (250−350 °C)) and tested at ambient temperature, the Orowan mechanism controlled the process when the precipitates grew above the critical radius. The experiment and theoretical prediction values are consistent for all samples tested at ambient temperature.

The measured yield strength increment at 573 K (300 °C) is exemplary included in Fig. 8 for comparison. As anticipated, the yield stress is considerably lower at 573 K (300 °C) than at ambient temperature. For both S40 and SZ40 samples at the peak aging condition and tested at elevated temperatures, the precipitate sizes remain notably small (1−2 nm), but the measured yield stress values are at least one order of magnitude lower than the theoretical values. Therefore, the shearing mechanism can be excluded as an operative strengthening mechanism at elevated temperature. In the Orowan bypass mechanism (Eq. (12)), the decrease in strength with increasing temperature may arise from the temperature dependence of the shear modulus G_m. Considering that G_m decreases from 25.4 GPa at ambient temperature to 21.1 GPa at 573 K (300 °C) for aluminum matrix (Table 4), the modified Orowan stress curve at 573 K (300 °C) as a function of the precipitate size is also included in Fig. 8. The Orowan stress at 573 K (300 °C) is generally shifted to a lower value than that at ambient temperature. However, the measured yield strength at 573 K (300 °C) remains much lower than the predicted ones, which indicates

that the classical Orowan bypass mechanisms cannot predict the precipitate strengthening effect at elevated temperature, and another strengthening mechanism should be involved.

4.3 Strengthening at elevated temperatures

A dislocation climb mechanism is invoked to explain the deformation at elevated temperatures (> $0.5T_m$) [35, 36]. Fig. 9 shows the theoretical yield stresses as a function of precipitate size at 573 K (300 °C) with S40 (0.24 vol.% Al_3Sc) as an example based on the dislocation climb and Orowan bypass mechanisms (Eqs. (8)-(13)). The parameters in the calculation are listed in Table 4, and the climb stresses are calculated using the distance y from r+2b and r+5b as the upper and lower boundaries, respectively. At elevated temperatures, the dislocation climb mechanism operates at stresses lower than the Orowan ones for an alloy with small and intermediate-sized precipitates (1-8 nm in radius). The strength increases with increasing precipitate size, which shows a contrary tendency to the Orowan mechanism in this size range. The predicted critical value of the precipitate radius is approximately 8 nm for the r+5b distance. For the large precipitate size (> 8 nm), the Orowan mechanism is dominant again.

In the dislocation climb model, the distance y between a precipitate center and a dislocation (see Fig. 7 and Eq. (4)) represents the initial point of a dislocation to climb a precipitate. In this study, the unit of the distance is considered the Burgers vector of aluminum matrix, b. In general, the distance required to climb a precipitate increases with the increasing temperature because the vacancy density in materials increases at higher temperature, which results in a lower energy required for the dislocation climb [42]. Moreover, the increase in precipitate size may lead to an increase in climb distance [38], which is related to the increased repulsive stress to a dislocation (Eqs. (4)-(9)). However, the precipitates Al_3(Sc, Zr) have less lattice misfit (1.07%) with

aluminum matrix than Al_3Sc (1.34%, see Table 4), which leads a lower strain field around the precipitate and consequently a lower y value. Thus, for S40, the distance y for the strength calculation is taken from r+2b to r+5b. For SZ40, considering the smaller precipitate size and less lattice misfit, the distance value is taken from r+b to r+2b when the precipitates are in the peak aging condition or limited coarsening (< 2 nm in radius), but the distances from r+2b to r+5b are used for the calculation to predict the strength at 623 K (350 °C), where the precipitate coarsening becomes obvious.

In fact, the size distribution of the precipitates varies over a wide range, particularly during the coarsening process. Fig. 10 shows an example of the precipitate size distribution of S40 after annealing at 573 K (300 °C) for 2000 hours. The particle size ranges from 1 nm up to 14 nm. It is worth mentioning that the critical coherent radius of Al_3Sc precipitates is around 15 nm [50] and the discussion below is based on the coherent precipitates. The increment of yield strength due to different precipitate sizes will be determined by the combination of dislocation climb and Orowan mechanisms at elevated temperature (see Fig. 10).

Because the precipitate coarsening behaviour generally follows Lifshitz-Slyozov-Wagner (LSW) function (see Figs. 3 and 10), the density function of the particles in a material, $f\left(\frac{r}{\bar{r}}\right)$, can be expressed as [25, 26, 51]:

$$f\left(\frac{r}{\bar{r}}\right) = \frac{4}{9}\left(\frac{r}{\bar{r}}\right)^2 \left(\frac{3}{3+\frac{r}{\bar{r}}}\right)^{\frac{7}{3}} \left(\frac{1.5}{1.5-\frac{r}{\bar{r}}}\right)^{\frac{11}{3}} e^{\left(\frac{\frac{r}{\bar{r}}}{\frac{r}{\bar{r}}-1.5}\right)}; \qquad 0 < \frac{r}{\bar{r}} < 1.5 \tag{16}$$

$$f\left(\frac{r}{\bar{r}}\right) = 0; \qquad \frac{r}{\bar{r}} \geq 1.5 \tag{17}$$

where r is the actual precipitate radius, and $\bar{r}$ is the mean precipitate radius. Because the function of dislocation climbing and Orowan bypass mechanisms are in parallel, strengthening is given by the smaller one of these two strengthening models. Then, the precipitate strengthening contribution of the two mechanisms can be described as follows:

$$\Delta\sigma_p = \int_0^{r_c} \Delta\sigma_c(r) f\left(\frac{r}{\bar{r}}\right) dr + \int_{r_c}^{1.5\bar{r}} \Delta\sigma_o(r)\, f\left(\frac{r}{\bar{r}}\right) dr \quad (18)$$

Both calculated increments in yield stresses (Eq. (18)) and experimental data of S40 and SZ40 at elevated temperatures are shown as a function of the precipitate size in Fig. 11. The yield strength increments of the S40 samples, which were annealed and tested at 523 K (250 ºC), are located in the calculated dislocation climbing zone using $y = r$+2b (Fig. 11a). In this zone, the strength increases with increasing precipitate size. When the samples were annealed for 2000 h and tested at 573 K (300 ºC, 0.61T_m), four experimental data points belonged to the dislocation climb zone with the r+2b and r+5b distance (Fig. 11b). At this temperature, the precipitates were coarsening. The mean Al_3Sc precipitate radius increases from 1.7 nm at the peak aging to 6.2 nm after 2000 h of annealing, which results in the shift of the dislocation climb distance from r+2b to r+5b. Thus, the yield strength of S40 at 573 K (300 ºC) slightly increases in the first 500 h of annealing and subsequently remains more and less stable (Fig. 6a).

To evaluate the possible Orowan mechanism for larger precipitates, the S40 samples were maintained at 723 K (450 ºC) for 45, 130 and 225 minutes to obtain large precipitate sizes of 7.5, 12.4, and 14.8 nm in mean radius, respectively; then, the samples were tested at 573 K (300 ºC), shown in Fig. 11b. It is interesting to observe that these experimental data fall into the Orowan operative zone, and the yield strengthen increment slightly decreases when the precipitate radius is larger than 7.5 nm, which indicates that the calculated and experimental data have consistent tendencies (Figs. 11a and b).

For the SZ40 samples that were tested at 573 K (300 ºC), four data points of the yield strength increment are located in the dislocation climb zone between the $r+b$ and $r+2b$ climb distances (Fig. 11c). The tested strength values do not significantly change, which is attributed to a similar precipitate size and no coarsening at 573 K (300 ºC). The experimental data at 623 K (350 ºC) are located in the calculated dislocation climb zone between $r+2b$ to $r+5b$ (Fig. 11d). At 623 K (350 ºC), the $Al_3(Sc, Zr)$ precipitates also become obviously coarsening, and the mean precipitate radius increases from 1.1 nm at peak aging to 5 nm after 2000 h of annealing. The increase in precipitate size increases the climb distance. In the dislocation climb zone (Fig. 11d), a larger precipitate size corresponds to higher strengthening effect, but a larger dislocation climb distance means a lower strengthening effect. Because of the synthesizing effect of precipitate coarsening and dislocation climb distance increase in the dislocation climb model, the yield strength of SZ40 at 623 K (350 ºC) remains approximately stable after the long-term annealing (Fig. 6b).

As previously mentioned, the classical precipitate shearing and Orowan bypass models can hardly predict the high-temperature strength of precipitation-strengthened materials. Using the dislocation climb model, the predicted yield stresses of S40 and SZ40 after the peak aging condition, tested at 523−623 K (250−350 ºC), are notably close the experimental data. The calculated values of S40 are located in the zone of the climb distance from $r+2b$ to $r+5b$, whereas they are in the zone from $r+b$ to $r+2b$ for SZ40, shown in Fig. 12. The strong decrease in yield strength of S40 and SZ40 at elevated temperatures (523−623 K (250−350 ºC)) (Fig. 4) is attributed to a lower strengthening efficiency of dislocation climb compared to precipitate shearing at ambient temperature.

It is evident that the dislocation climb model indeed predicts the trend of much lower yield stresses at high temperature for small and intermediate-sized precipitates (1-8 nm in radius)

compared to ambient temperature. For larger precipitates (> 8-10 nm), the Orowan mechanism with modified G_m can predict the high-temperature yield strength. The high-temperature experimental data of S40 and SZ40 at peak aging and during the long-term annealing (precipitate coarsening) are fairly consistent with the theoretical prediction, which provides a conceptual understanding about the mechanical behavior at high temperature. However, there is no literature and experimental value for the dislocation distance y as a function of temperature and precipitate size in the dislocation climb model. With simplified assumptions in the model, the accuracy of the predictions is certainly affected to some extent.

4.4 Prospect of dislocation climb and Orowan mechanisms for high-temperature applications

For Al-based materials that are alloyed with Sc and Zr and exposed to high temperature (> 0.6*Tm*), the coarsening of Al_3Sc and Al_3(Sc, Zr) precipitates are often inevitable. The strength variation with coarsening precipitates at high service temperature are major concerns for material design and application. Fortunately, the high-temperature strength of such materials is more tolerable for large precipitate size caused by the coarsening process. For the best strength at high temperatures (573–623 K (300–350 ºC)), the optimal precipitate radius is approximately 7–9 nm for S40 and SZ40 (Figs. 11b and d). On the contrary, the highest strength at ambient temperature is achieved at the precipitate radius of approximately 2 nm (Fig. 8). At the intermediate size range (4-14 nm), the high-temperature strength only moderately changes with the precipitate size, which is predicted by the proposed dislocation climb and Orowan models (Fig. 11 b and d). For example, the yield strength increment of S40 at 573 K (300 ºC) (r+5b) changes from 44 MPa with $\bar{r}$ = 4 nm to 33 MPa with $\bar{r}$=14 nm. Using the coarsening rate constant a = 3.16×10^{-32} m^3s^{-1} at 573 K (300 ºC) (Fig. 3), it may take a total of 23 558 h as Al_3(Sc) precipitates grows up

from 4 nm to 14 nm. SZ40 has a similar trend. The predicted strength increment (r+5b) at 623 K (350 ºC) is approximately 39 MPa with $\bar{r}$ = 4 nm. When Al_3(Sc, Zr) precipitates coarsen to $\bar{r}$ = 14 nm, the strength increment only changes to 38 MPa. Using the coarsening rate $a = 1.19\times10^{-32}$ m^3s^{-1} at 623 K (350 ºC), it takes approximately 62 558 h to increase the precipitate radius from 4 nm to 14 nm. In addition, for coarser precipitates (>14 nm), the yield strength at high temperatures only slightly decreases according to the Orowan operative mechanism (Figs. 11 b and d), which provides a good safety margin for materials with a slow coarsening rate at high temperature.

Previous studies [10, 30] found that the creep resistance of AlSc(Zr) alloys at elevated temperature (573 K (300 ºC)) increased with increasing precipitate radius, and the optimal creep resistance occurred at the precipitate radii of 6 to 9 nm, which was explained using the dislocation climb mechanism. Similar to the creep resistance, the high-temperature strength of Al_3Sc and Al_3(Sc, Zr) with Al-B_4C composites is also less sensitive to coarse precipitates. With a low coarsening rate of Al_3Sc and Al_3(Sc, Zr), Al-B_4C composites with Sc and Zr are expected to perform well during prolonged exposure at elevated service temperatures. The tolerance of the precipitate coarsening (maximum allowable precipitate radius) depends on the usage temperature and duration, because the overall performance of a material is a trade-off between both mechanical properties at ambient and high temperatures. The proposed dislocation climb and Orowan mechanisms in this work provide an insight of the precipitate strengthening at high temperature and a guide for further Al-B_4C composite design.

5. Conclusions

1) The presence of large B_4C particles (15 vol.% with average size 23 μm) has a moderate strengthening effect on Al-B_4C composites. The yield strength contribution of 15 vol.% B_4C is approximately 12 MPa at ambient temperature and remains about 10 MPa at 573 K (300 °C). The precipitation of nanoscale Al_3Sc and Al_3(Sc, Zr) in the composite matrix provides a significant and predominate contribution to the composite strength at both ambient and elevated temperatures.

2) During long-term thermal annealing, the Al_3Sc precipitates in the composite with Sc (S40) remain coarsening-resistant at 523 K (250 °C), whereas the Al_3(Sc, Zr) precipitates in the composite with Sc and Zr (SZ40) are thermally stable at 573 K (300 °C). At higher annealing temperatures (573 K (300 °C) for S40 and 623 K (350 °C) for SZ40), both Al_3Sc and Al_3(Sc, Zr) precipitates coarsen with increasing annealing time. The yield strengths of S40 and SZ40 at ambient temperature decrease with increasing precipitate size, which can be explained by the classical precipitate shearing and Orowan bypass mechanisms.

3) The yield strengths of S40 at 523 (250) and 573 K (300 °C) slightly increase in the first 500 h of annealing and subsequently remain constant till 2000 hours, whereas the yield strengths of SZ40 at 573 (300) and 623 K (350 °C) are always stable up to 2000 hours. At elevated temperatures, the yield strengths of S40 and SZ40 become approximately independent of precipitate coarsening, which can be described and predicted by the dislocation climb mechanism.

4) The dislocation climb mechanism is invoked to explain the yield strength at elevated temperatures (> $0.5T_m$). The dislocation climb and Orowan bypass mechanisms are proposed as the governing strengthening mechanisms for high-temperature mechanical properties. The combination of dislocation climb and Orowan models can explain the lower strengthening

efficiency of coherent precipitates and the stable strength with coarse precipitates at high temperature compared to those at ambient temperature. The predicted yield strengths at elevated temperatures are consistent with the experimental data of S40 and SZ40 composites.

Acknowledgments

The authors would like to acknowledge the financial support of the Natural Sciences and Engineering Research Council of Canada (NSERC) and Rio Tinto Aluminum through the NSERC Industry Research Chair in the Metallurgy of Aluminum Transformation at University of Quebec at Chicoutimi.

References

1. X.G. Chen: Application of Al-B_4C Metal Matrix Composites in the Nuclear Industry for Neutron Absorber Materials. In: N. Gupta and W.H. Hunt, (Ed.). Solidification Processing of Metal Matrix Composites, TMS 2006. p.343-350.
2. G. Bonnet, V. Rohr, X.G. Chen, J.L. Bernier, R. Chiocca, H. Issard: *Packag. Transp. Stor. Secur. Radioact. Mater.*, 2009, vol. 20, pp. 98-102.
3. J.X. Deng, J.L. Sun: *Ceram. Int.*, 2009, vol. 35, pp. 771-78.
4. J.G. Kaufman, *Properties of aluminum alloys: tensile, creep, and fatigue data at high and low temperatures*, ASM International, USA, 1999.
5. R.W. Hyland: *Metall. Trans. A*, 1992, vol. 23, pp. 1947-955.
6. J. Royset, N. Ryum: *Int. Mater. Rev.*, 2005, vol. 50, pp. 19-44.
7. J. Lai, Z. Zhang, X.G. Chen: *Mat. Sci. Eng. A*, 2012, vol. 532, pp. 462-70.
8. C.B. Fuller, D.N. Seldman: *Acta Mater.*, 2005, vol. 53, pp. 5415-428.
9. V.I. Yelagin, V.V.Zakharov, S.G.Pavlenko, T.D. Rostova: *Phys.Met. Metall.*, 1985, vol. 60, pp. 88-92.

10. C.B. Fuller, D.N. Seidman, D.C. Dunand: *Acta Mater.*, 2003, vol. 51, pp. 4803-814.

11. Y.W. Riddle, T.H. Sanders: *Metall.Mater. Tran. A*, 2004, vol. 35A, pp. 341-50.

12. N.A. Belov, A.N. Alabin, D.G. Eskin, V.V. Istomin-Kastrovskii: *J. Mater. Sci.*, 2006, vol. 41, pp. 5890-899.

13. E. Clouet, A. Barbu, L. Laé, G. Martin: *Acta Mater.*, 2005, vol. 53, pp. 2313-325.

14. A. Tolley, V. Radmilovic, U. Dahmen: *Scr. Mater.*, 2005, vol. 52, pp. 621-25.

15. B. Forbord, W. Lefebvre, F. Danoix, H. Hallem, K. Marthinsen: *Scr. Mater.*, 2004, vol. 51, pp. 333-37.

16. Y. Harada, D.C. Dunand: *Mater. Sci. Eng. A*, 2002, vol. 329, pp. 686-95.

17. K.E. Knipling, D.C. Dunand, D.N. Seidman: *Z. Metallkd.*, 2006, vol. 97, pp. 246-65.

18. X.G. Chen, L. St-Georges, M. Roux: *Mater. Sci. Forum*, 2012, vol. 706-709, pp. 631-37.

19. J. Lai, Z. Zhang, X.G. Chen: *Mater. Sci. Tech.*, 2012, vol. 28, pp. 1276-286.

20. N. Chawla, Y-L Shen: *Adv. Eng. Mater.*, 2001, vol. 3, pp. 357-70.

21. J. Lai, Z. Zhang, X.G. Chen: *J. Alloy Compd.*, 2013, vol. 552, pp. 227-35.

22. Z. Zhang, K. Fortin, A. Charette, X.G. Chen: *J. Mater. Sci.*, 2011, vol. 46, pp. 3176-185.

23. J. Lai, Z. Zhang, X.G. Chen: *J. Mater. Sci.*, 2011, vol. 46, pp. 451-59.

24. P.M. Kelly: *Met. Forum*, 1982, vol. 5, pp. 13-23.

25. I.M. Lifshitz, V.V. Slyozov: *J. Phys. Chem. Solids*, 1961, vol. 19, 35-50.

26. C. Wagner: *Z. Elektrochem.*, 1961, vol. 65, pp. 581-91.

27. A.J. Ardell: *Metall. Trans. A*, 1985, vol. 16, pp. 2131-165.

28. Y. Harada, D.C. Dunand: *Scr. Mater.*, 2003, vol. 48, pp. 219-22.

29. Y. Touloukian: Thermophysical Properties of High Temperature Solid Materials, Macmillan, New York, 1967.

30. D.N. Seidman, E.A. Marquis, D.C. Dunand: *Acta Mater.*, 2002, vol. 50, pp. 4021-35.

31. J. Rosler: *Int. J. Mater. Prod. Tec.*, 2003, vol. 18, pp. 70-90.

32. E. Nembach: Particle strengthening of metals and alloys, first ed., Wiley, New York, 1996.

33. E.A. Marquis, D.N. Seidman, D.C. Dunand: *Acta Mater.*, 2003, vol. 51, pp. 4751-760.

34. R.A. Karnesky, L. Meng, D.C. Dunand: *Acta Mater.*, 2007, vol. 55, pp. 1299-1308.

35. E.A. Marquis, D.C. Dunand: *Scr. Mater.*, 2002, vol. 47, pp. 503-8.

36. R.W. Cahn, P. Haasen: Physical Metallurgy,fourth ed., North Holland, Netherlands, 1996.

37. Y. Miura, M. Nakayama, A. Furuta: *JIM (The Japan Institute of Metals)*, 1993, pp. 255-65.

38. M.E. Krug, D.C. Dunand: *Acta Mater.*, 2011, vol. 59, pp. 5125-134.

39. J. Dundurs, Mathematical theory of dislocations, ASME, New York, 1969, pp. 70-115.

40. M.A. Meyers, K.K. Chawla: Mechanical metallurgy: principles and applications, first ed., Prentice-Hall Inc., New Jersey, 1984.

41. B. Jansson, A. Melander: *Scr. Metall. Mater.*, 1978, vol. 12, pp. 497-98.

42. G.E. Dieter, D. Bacon: Mechanical metallurgy, McGraw-Hill, London, 1988.

43. C. Fu, Electronic: *J. Mater. Res.*, 1990, vol. 5, pp. 971-79.

44. K. Fukunaga, T. Shouji, Y. Miura: *Mat. Sci. Eng. A*, 1997, vol. 239-240, pp. 202-5.

45. E.P. George, D.P. Pope, C.L. Fu, J.H. Schneibel: *ISIJ Int.*, 1991, vol. 31, pp. 1063-75.

46. R.W. Hyland Jr, R.C. Stiffler: *Scr. Mater.*, 1991, vol. 25, pp. 473-7.

47. H.J. Frost, M.F. Ashby: Deformation-mechanism maps: the plasticity and creep of metals and ceramics, Pergamon Press, New York, 1982.

48. M.E. Drits, L.S. Toropova, Y.G. Bykov, F.L. Gushchina, V.I. Elagin, Y.A. Filatov: *Russ. Metall.*, 1984, vol. 1, pp.83.

49. D. Tabor: *J. I. Met.*, 1951, vol. 79, pp. 1-18.

50. S. Iwamura, Y. Miura: *Acta Mater.*, 2004, vol. 52, pp. 591-600.

51. M. Tiryakioğlu, G. Ökten, D. Hudak: *J. Mater. Sci.*, 2009, vol. 44, pp. 5754-759.

A List of Figure Captions

Fig. 1. Optical microstructure of S40 composite at the peak aging: (a) low magnification and etched sample and (b) high magnification.

Fig. 2. TEM dark field images showing precipitates: S40 on peak aging condition (a); 2000 h annealing at 523 K (250 °C) (b); 2000 h annealing at 573 K (300 °C) (c); SZ40 on peak aging condition (d); 2000 h annealing at 573 K (300 °C) (e); and 2000 h annealing at 623 K (350 °C) (f).

Fig. 3. Precipitate coarsening as a function of annealing time at 523 K (250 °C) and 573 K (300 °C) for S40 (a) and at 573 K (300 °C) and 623 K (350 °C) for SZ40 (b).

Fig. 4. Yield strengths of S40, SZ40, the base composite (Al-15%B_4C) and AA1100 at various test temperatures (a) as well as true stress–strain curves of the base composite (b), S40 (c) and SZ40 (d) obtained from compression tests in different conditions. * The data of AA1100 are from the reference [4].

Fig. 5. Vickers microhardness, measured at ambient temperature, after the composites annealed at elevated temperatures for different holding time: (a) S40 and (b) SZ40.

Fig. 6. Yield strength, measured at the same elevated temperature as the annealing temperature, as a function of annealing time: (a) S40 and (b) SZ40.

Fig. 7. Three-dimensional schematic showing an edge dislocation to climb a particle (a) and the side view (b). The dislocation 1 is located at the position: $z=z_0+h$ and $y=cos\theta(r+nb)$, and the dislocation 2 is on the position with a maximum repulsion force.

Fig. 8. The calculated (shearing and Orowan mechanisms) and experimental strength data at 298 K (25 °C) as a function of mean precipitates for S40 (a) and SZ40 (b). The measured values in strength increments at elevated temperatures (573 K (300 °C)) are also included for comparison.

Fig. 9. Theoretical calculation of yield stresses based on the models of dislocation climb and Orowan mechanisms for S40 (0.24 vol.% Al_3Sc) at 573 K (300 °C) as a function of precipitate

radius. The distance, y=r+2b or r+5b, are used in the dislocation climb model (see Fig. 7).

Fig. 10. Precipitate size distribution and LSW simulation in S40 annealing at 573 K (300 °C) for 2000 h.

Fig. 11. The calculated yield strength increments and experimental strength data as a function of the mean precipitate radius: for S40 at 523 K (250 °C) (a) and 573 K (300 °C) (b); for SZ40 at 573 K (300 °C) (c) and 623 K (350 °C) (d).

Fig. 12. Calculated yield strength increments and experimental data after the peak aging tested at 523−623 K (250−350 ºC) for S40 (a) and SZ40 (b).

A List of Tables

Table 1 Nominal chemical composition of experimental composites

Code	Element (wt.%)				
	Sc	Zr	Ti	B_4C (vol.%)	Al
Base composite	−	−	1.50	15	
S40	0.40	−	1.50	15	Balance
SZ40	0.40	0.24	1.50	15	

Table 2 Peak aging and annealing parameters

Code	Aging		Annealing	
	T (K/°C)	Time (h)	T (K/°C)	Time (h)
S40	573 (300)	24	523 (250)	up to 2000
			573 (300)	up to 2000
SZ40	573 (300)	24	573 (300)	up to 2000
			623 (350)	up to 2000

Table 3 Yield strengths measured at different test temperatures

Test temperature, K (°C)	Yield strength (MPa)		
	S40	SZ40	Base composite
298 (25)	141.3±10.8	165.4±13.9	45.8±1.1
523 (250)	59.3±1.6	71.9±2.6	31.6±0.9
573 (300)	46.0±1.9	54.0±1.6	25.2±2.0
623 (350)	39.3±1.1	39.2±1.6	18.4±0.5

Table 4 Constants used in the calculations.

T (K/°C)	G_m[1*] (GPa)	G_p[2*] (GPa)	b[3*] (Å)	δ-S40[4*]	δ-SZ40[4*]	v_m	v_p
298 (25)	25.4 [16]	69 [46]	2.86 [16]	1.34% [16]	1.07% [16]		
523 (250)	22.4	66.8	2.87	1.17%	0.90%		
						0.34 [46]	0.2 [43]
573 (300)	21.1 [16]	66.2	2.88	1.14%	0.87%		
623 (350)	21.0	65.7	2.88	1.10%	0.83%		

[1*] Temperature dependence of the shear modulus is given by $-13.6\ \mathrm{MPa\cdot K^{-1}}$ for Al [47].

[2*] Temperature dependence of the Young's modulus is given by $-26\ \mathrm{MPa\cdot K^{-1}}$ [48].

[3*] Thermal expansion coefficient value of Al is $24.7\times10^{-6}\ \mathrm{K^{-1}}$ [29].

[4*] Thermal expansion coefficient value of $16\times10^{-6}\ \mathrm{K^{-1}}$ for Al_3Sc [16].

List of Figures

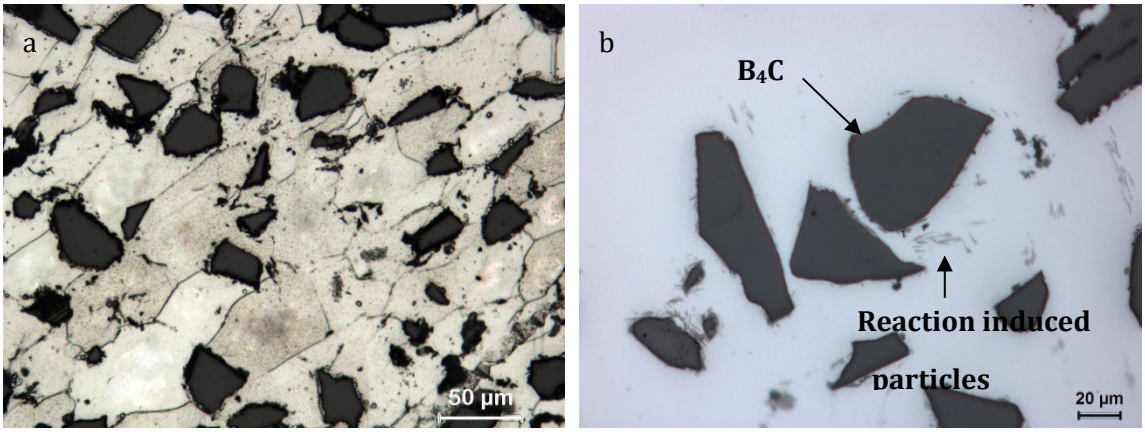

Figure 1

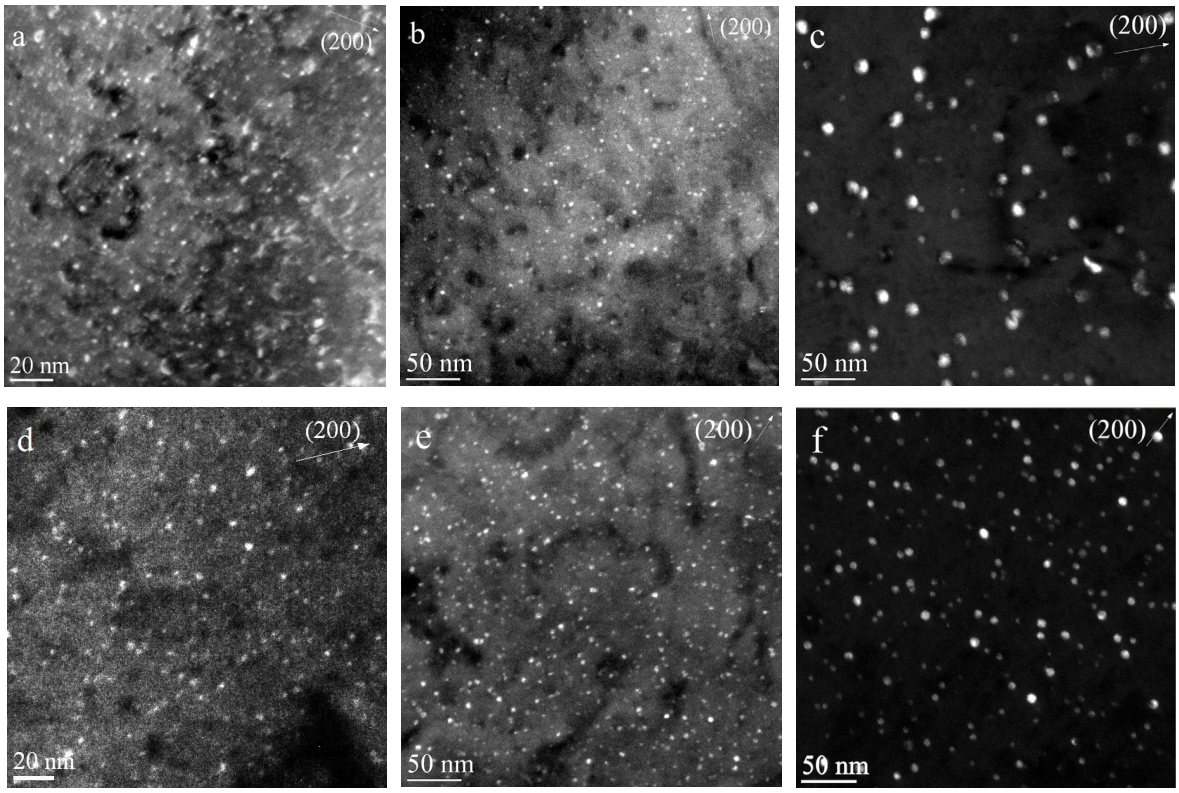

Figure 2

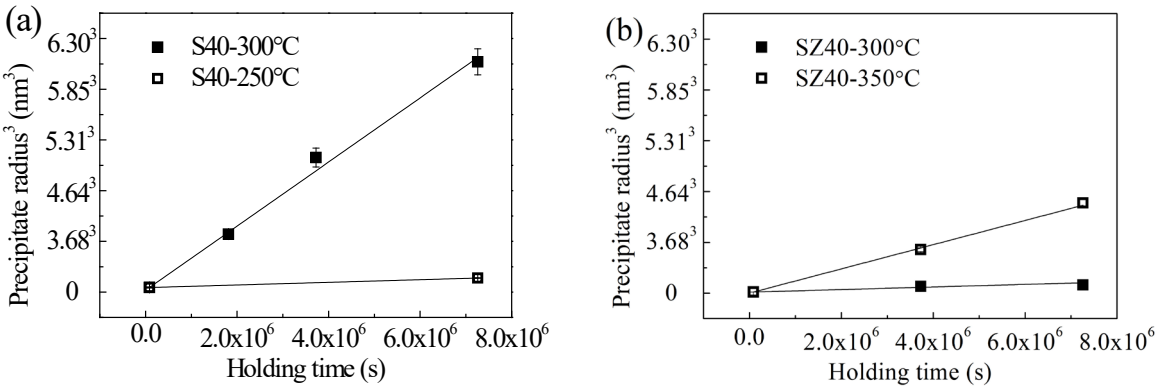

Figure 3

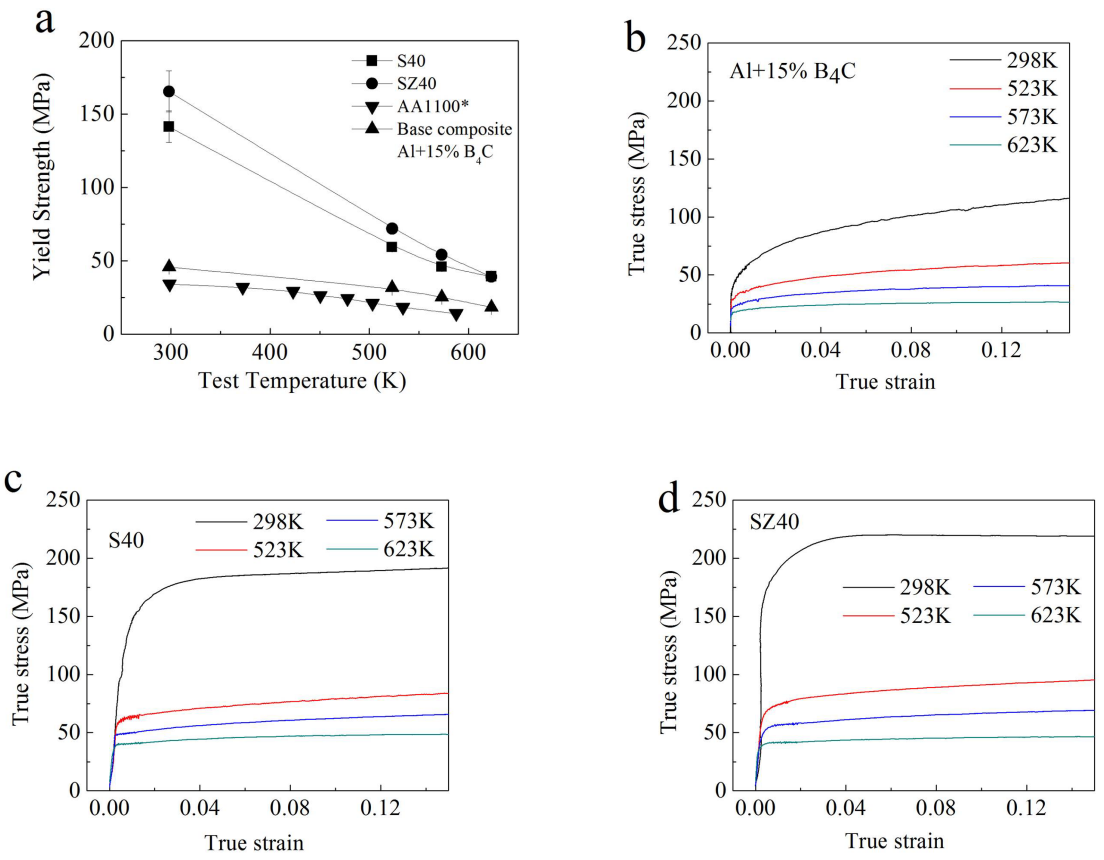

Figure 4

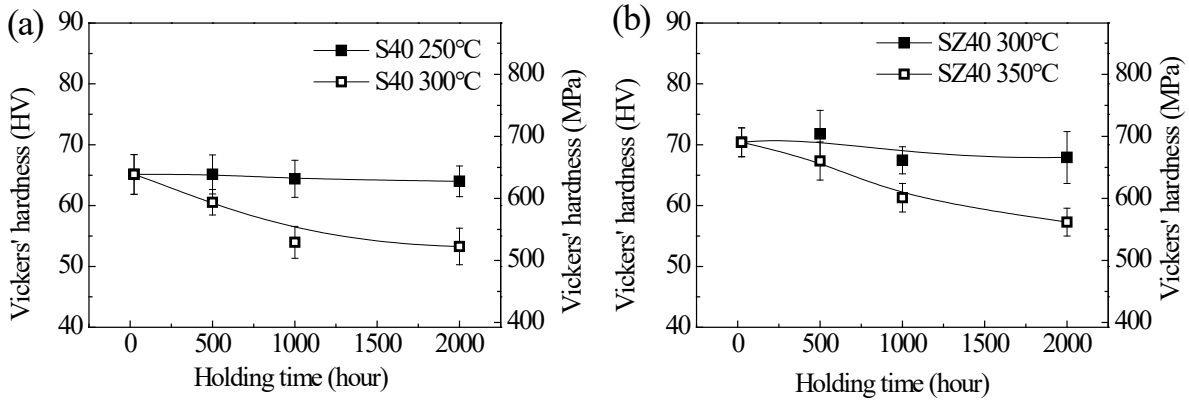

Figure 5

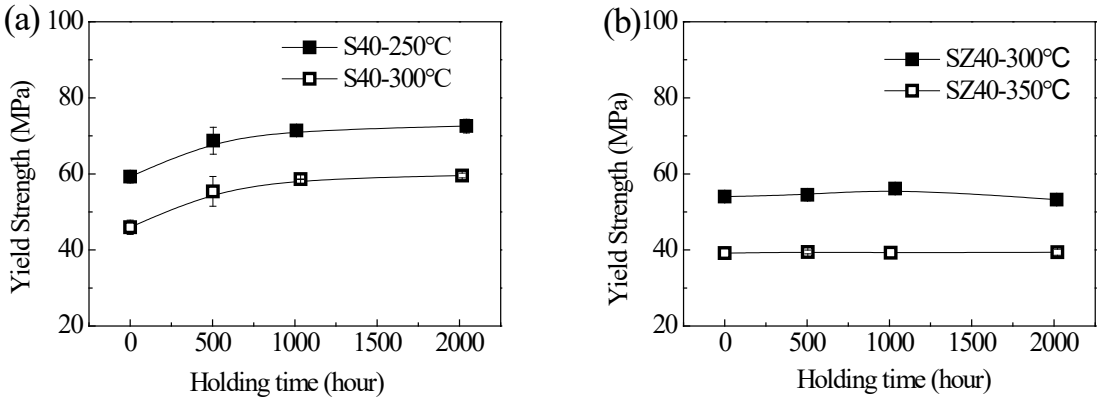

Figure 6

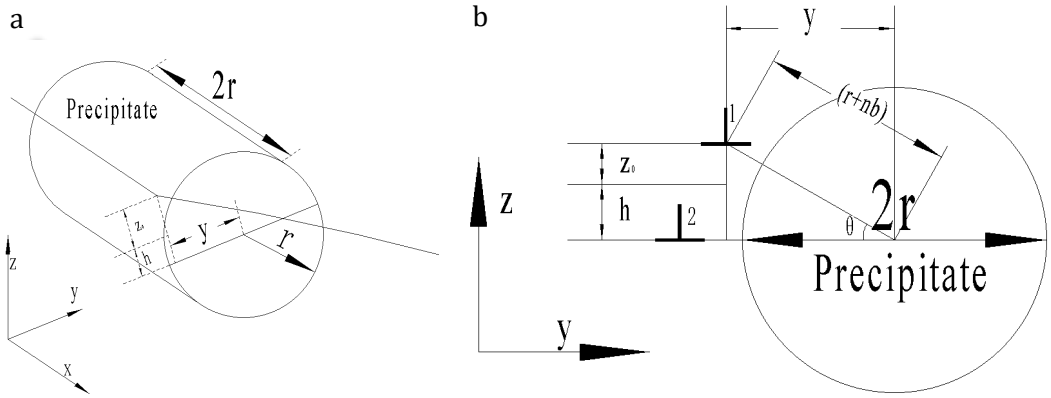

Figure 7

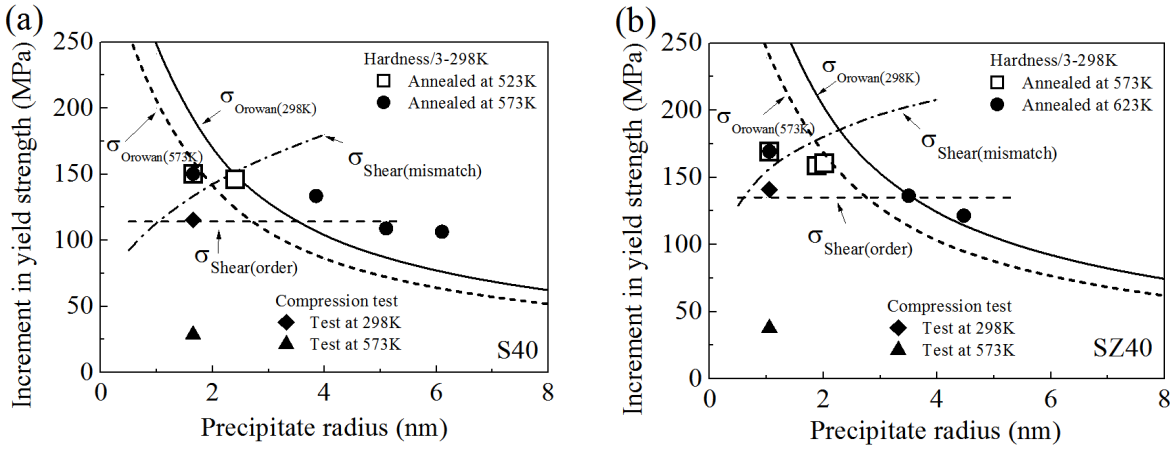

Figure 8

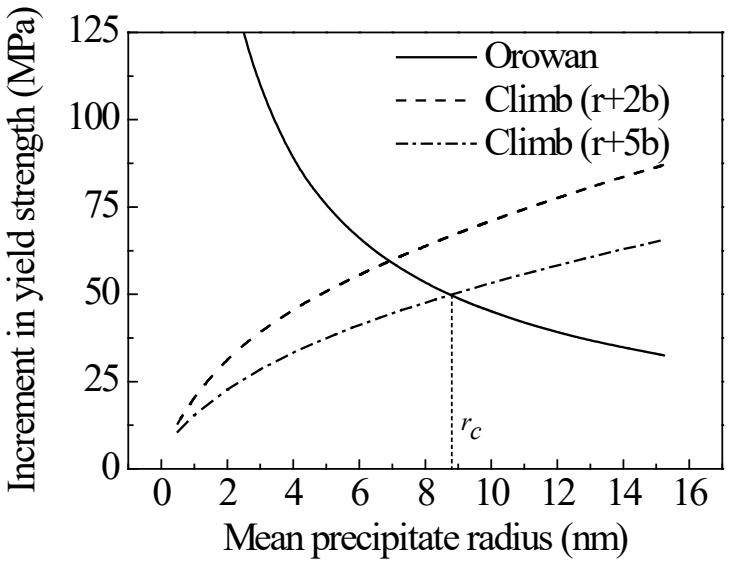

Figure 9

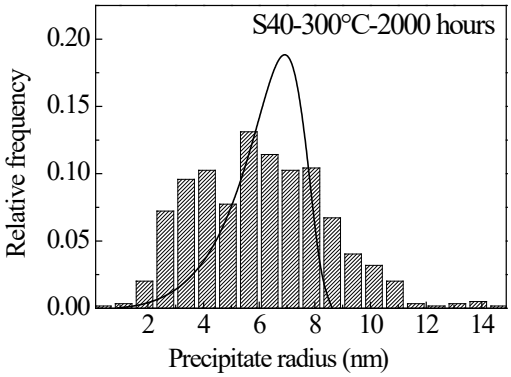

Figure 10

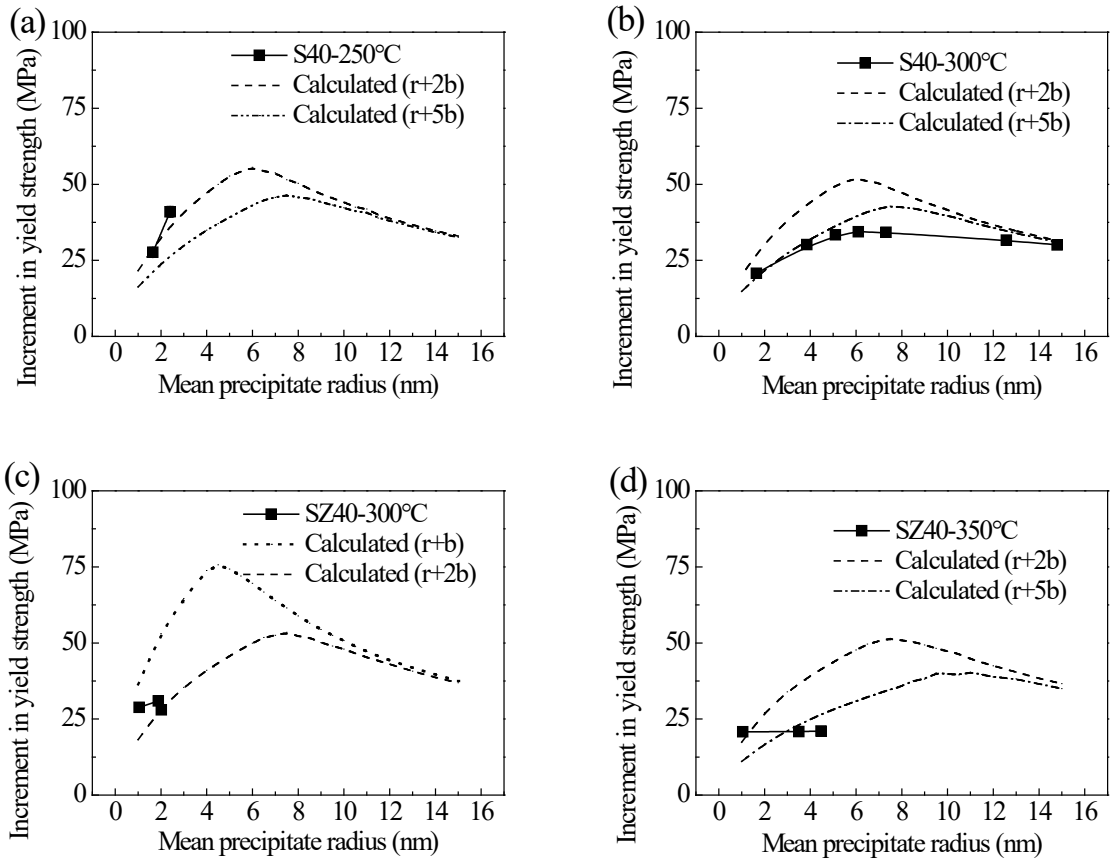

Figure 11

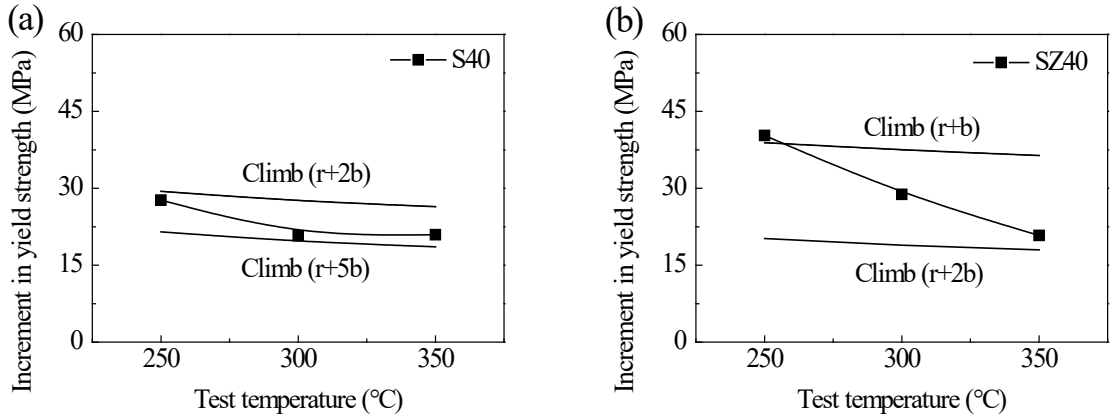

Figure 12